Materials Today Communications 52 (2026) 114951

Contents lists available at ScienceDirect

Materials Today Communications

journal homepage: www.elsevier.com/locate/mtcomm

A novel flexible magnetorheological fluid polishing needle for polishing slender bend tube

Dawei Gao [a], Yifan Xu [a], Chen Jiang [a,*], Rui Gao [b,*]

[a] College of Mechanical Engineering, University of Shanghai for Science and Technology, Shanghai 20093, China
[b] State Key Laboratory of Ultra-precision Machining Technology, Department of Industrial and Systems Engineering, The Hong Kong Polytechnic University, Hong Kong, China

ARTICLE INFO

Keywords:
Slender tubes
Magnetorheological fluid
Finishing
Finite element simulation
Ultra-precision machining

ABSTRACT

The demand for ultra-precision finishing of the inner surfaces of slender bend tubes is increasing in advanced manufacturing. However, achieving high-quality surface finishes in such confined geometries remains a significant challenge due to limited accessibility and the complexity of tube shapes. To address these limitations, this study proposed a novel flexible polishing needle based on magnetorheological fluid (MRF) technology with added dispersant. The polishing needle, composed of magnets constrained by a coil spring, was systematically optimized in terms of magnet shape and arrangement through finite element (FE) simulations and experiments. The results demonstrated that the optimized magnet configuration could significantly improve both efficiency and surface quality. Experimental polishing of both straight and bent 304 stainless steel tubes showed that the average surface roughness (Ra) was reduced from 1.24 to 2.28 μm to 0.40–0.62 μm after polishing 30 min. Furthermore, the method proved effective for tubes with bend angles ranging from 15° to 90°, significantly improving both surface quality and flow efficiency. This research provides a versatile and effective solution for the polishing of slender tubes with complex geometries, offering substantial potential for practical applications in high-end manufacturing.

1. Introduction

Slender tubes are widely used in industries such as aerospace, medical devices, and chemical engineering [1–3]. In these fields, the quality of the tube's inner surface plays a vital role in determining system performance, durability, and safety [4,5]. Conventional manufacturing methods, including drawing, machining, and additive manufacturing, often result in poor internal surface finishes [6]. Moreover, the geometry of these slender tubes makes it particularly difficult to achieve effective polishing of the inner surface. Therefore, developing efficient techniques for polishing the inner surface of slender tubes is essential to meet the demanding requirements of modern applications.

Various methods have been explored for polishing the inner surfaces of tubes, with free-abrasive techniques such as abrasive flow machining (AFM) [7–9], electrochemical polishing (ECP) [10–12], and abrasive jet polishing (AJP) [13–15], is the most widely used due to its adaptability to complex geometries and confined spaces. A self-formulated abrasive flow liquid with high viscosity has been utilized to finish tube runner surfaces, effectively removing burrs and the hard recast layer produced by electrical discharge machining (EDM) [16]. To improve process efficiency, a semi-mechanistic model for two-phase AFM was developed, integrating fluid flow, wall slip, and process evolution sub-models; this approach was validated through experiments on 20 × 10 mm titanium alloy ellipsoidal tubes [17]. Further optimization of two-phase AFM was achieved by Liu et al. [18], who conducted a full factorial experiment to investigate the effects of particle density, particle size, and abrasive viscosity, resulting in optimized parameters for polishing micro-holes in non-linear tubes. For tubes produced by additive manufacturing, Duval-Chaneac et al. [19] demonstrated that the use of four different polishing slurries could reduce the surface roughness (Sa) of workpieces from an initial 14 μm to approximately 2 μm. Li et al. [20] applied concentrated suspension theory and improved the existing Preston model to elucidate the material removal mechanism. In the case of Inconel 718 tubes, ECP reduced the inner surface roughness from 6.05 μm to 3.66 μm, although a decrease in surface hardness and elastic modulus was observed [21]. Wu et al. [22] introduced a gradient voltage ECP strategy for polishing additively manufactured 316 stainless steel tubes, achieving a surface roughness (Ra) of approximately 1 μm.

* Corresponding authors.
E-mail addresses: jc_bati@163.com (C. Jiang), rui-gao.gao@polyu.edu.hk (R. Gao).

https://doi.org/10.1016/j.mtcomm.2026.114951
Received 8 December 2025; Received in revised form 24 February 2026; Accepted 3 March 2026
Available online 5 March 2026

Barletta et al. [23] systematically investigated the effects of abrasive jet speed, machining cycle, and abrasive mesh size on surface roughness and material removal during AJP of high-strength aluminum alloy tubes with a 10 mm diameter. Subsequently, a soft abrasive rotating jet polishing (SARJP) method was proposed, reducing the average surface roughness of stainless steel tube inner walls from 1.05 μm to 0.212 μm under optimal conditions [24]. Building on this, a recent study employed an integrated multi-objective optimization algorithm based on CatBoost and AGE-MOEA, enabling simultaneous prediction and optimization of surface roughness and material removal rate for the inner surfaces of circular tubes using SARJP [25].

In recent years, magnetic abrasive finishing (MAF) has emerged as a promising alternative for inner surface polishing, utilizing a flexible abrasive medium composed of magnetic particles [26–28]. For example, Verma et al. [29] developed a system using two permanent magnets with like poles facing each other, creating a high magnetic flux density around the circumferential area between the magnets and achieving effective polishing results on stainless steel tubes. Singh et al. [30] applied the MAF method to brass tubes, demonstrating that, with optimized process parameters, a minimum average surface roughness of 0.51 μm could be achieved after 60 min of polishing. In addition, magnetorheological finishing (MRF) and magnetic compound fluid (MCF) are notable for their high viscosity and uniform particle dispersion [31–33]. These characteristics allow them to form flexible, adaptive polishing tools under an external magnetic field [34,35]. In 2007, Nishida et al. [36] applied MCF, a mixture of magnetic fluid (MF) and MRF, to polish the inner walls of capillary tubes. They subsequently investigated how the flow direction of abrasive particles [37] and the use of a pulsed magnetic field [38] affect polishing performance. Under a rotating magnetic field, the continuous renewal of abrasive particles in the MCF slurry enabled a surface roughness of Ra 6.4 nm to be achieved in capillary tubes [39]. In further work, hydrogen peroxide (H_2O_2) and malic acid (MA) were added to the MCF slurry for polishing titanium capillary tubes, reducing surface roughness from Ra 3.10 μm to Ra 65.3 nm [40]. These results highlight the potential of magnetic field-assisted polishing for internal finishing of slender tubes. However, its application to tube interior polishing remains limited. In particular, there is a notable lack of study on slender tubes with a length-to-diameter ratio greater than 25, especially when the tubes include complex bends.

This study introduces a novel flexible polishing needle utilizing MRF technology for the polishing of inner surfaces in slender bent tubes. Polishing performance was evaluated through a combination of numerical simulations and experimental validation. The working principle of the proposed MRF polishing needle is presented, followed by an investigation of the polishing mechanism using finite element (FE) simulation and experiments. The shape and arrangement of the magnets were optimized to enhance polishing efficiency. The feasibility of the optimized polishing needle was further assessed on various slender bent tubes, resulting in significant improvements in surface quality. These findings demonstrate that the proposed method provides an effective solution for polishing the inner surfaces of slender bent tubes and offers a reliable technical reference for future research in inner surface treatment processes.

2. Methodology

2.1. Principle of flexible MRF polishing needle

Fig. 1 illustrates the operating principle of the MRF polishing needle designed for finishing the inner surfaces of slender tubes. As depicted in Fig. 1(a), the polishing needle comprises permanent magnets linked by a coil spring and held in place by a clamp. To enhance needle flexibility and prevent damage to the encapsulating layer, a spherical magnet shape was selected.These beads are in direct contact with each other, aligned along the z axis of the needle without any physical spacers, forming a continuous magnetic structure.The mandrel's inner diameter aligns with the maximum horizontal diameter of the magnetic beads, while the spring wire has a diameter of 0.2 mm, providing essential flexibility for conforming to curved tube geometries. The spring extends 20–30 mm beyond the tube exit to interface with the spindle while still enabling full traversal of the tube length. The diameter of polishing needle is around 2 mm. The clamp is mounted on a motor spindle, enabling rotation of the entire assembly. To prevent damage to the tube's inner wall during polishing, a layer of polyolefin heat shrink tubing is fitted over the spring. Additionally, the spring imparts the required flexibility, allowing the polishing needle to conform to the tube's geometry. For tubes longer than the polishing needle, simultaneous axial translation along the tube length ensures complete internal machining.

The polishing slurry is injected into the tube. Fig. 1(b) shows that when an external magnetic field is applied, the carbonyl iron particles (CIP) within the fluid align along the magnetic field lines, forming chain-like structures. The addition of α-cellulose increases the viscosity of the fluid, which enhances its ability to shear and aggregate particles. The dispersant ensures that the polishing fluid remains well-dispersed, even

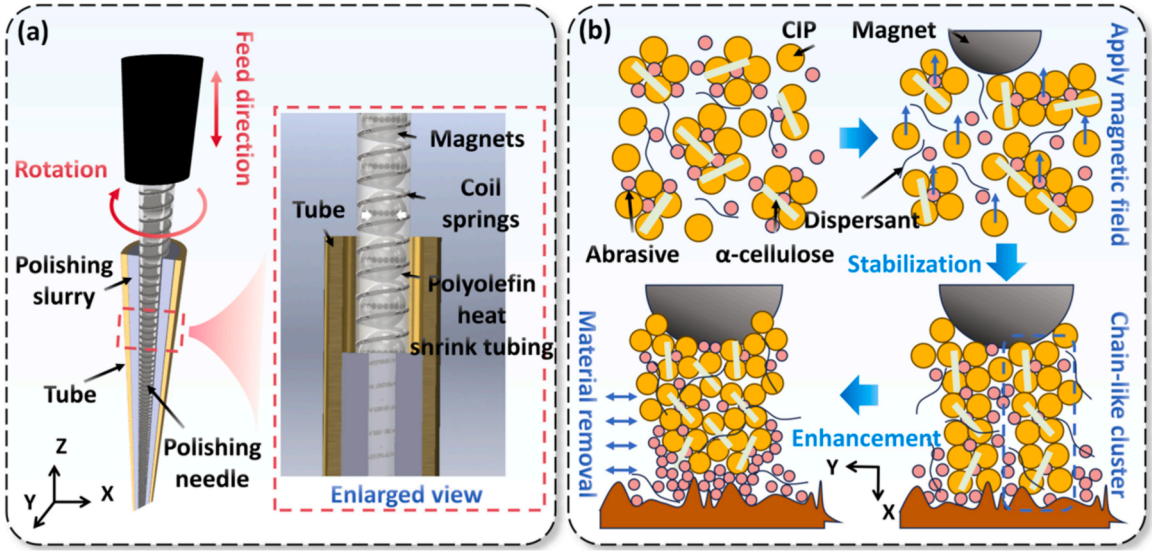

Fig. 1. Schematic diagram of the proposed polishing principle. (a) Flexible polishing needle diagram. (b) State of MRF under an applied magnetic field.

under dynamic magnetic conditions, thereby maintaining particle stability and consistent polishing performance.

The mechanical behavior of the polishing fluid changes in response to the magnetic field. Without the field, the fluid behaves like a Newtonian liquid [41]. However, when the magnetic field is applied, it exhibits non-Newtonian, Bingham fluid characteristics. This transition is described by the rheological equation [42], which models the fluid's macroscopic properties shown in Eq. (1).

$$\tau = \eta \bullet \gamma + \tau_0 \sin(\gamma), |\tau| > |\tau_0|$$

$$\gamma = 0, \quad |\tau| < |\tau_0| \tag{1}$$

Where τ is shear stress, η is initial viscosity of slurry, γ is shear rate, τ_0 is yield stress. Under the rotating magnetic field, the abrasive particles primarily interact with the tube's inner surface through a combination of applied normal force and shear stress. This mechanical action effectively removes material and achieves the desired polishing effect.

2.2. Magnetic flux density modelling

This section presents a simplified theoretical framework using a single spherical magnetic bead as a model system. The purpose is to illustrate the fundamental physical principles governing the magnetic field, prior to introducing the numerical methods used for the actual, more complex geometries in our simulations and experiments. The effectiveness of magnetic field-assisted polishing is closely linked to the strength and distribution of the magnetic field. To accurately model the magnetic field, several assumptions are made. First, the permanent magnet is uniformly magnetized. According to Ampere's law [43], the relationship between magnetic flux density and the surface current density is established:

$$\boldsymbol{B} = \frac{\mu_0}{4\pi} \oint_s \frac{J_s R}{R^3} ds \tag{2}$$

Where $\boldsymbol{B}$ is magnetic flux density, μ_0 is permeability of free space, J_s is surface current density, R is the distance between any two points in space.

Building on Ampere's molecular current hypothesis, each unit of a permanent magnet can be represented as a circular current. At the edges of the magnet's cross-section, some current segments remain uncanceled, which collectively form a large circular current along the perimeter. The lateral surface magnetization current density of the permanent magnet is related to the magnetization and the unit normal vector of the magnetic medium's surface [44].

$$J_s = \vec{M} \times \vec{n} \tag{3}$$

where M is magnetization, n is the unit normal vector of the magnetic medium's surface. The magnetic field generated by a single spherical magnet is analyzed using spherical coordinates, as illustrated in Fig. 2. In this model, Point A denotes a location on the surface of the spherical magnet, while Point P represents a point outside the magnet.

According to Eq. (4), the equivalent circular current density on the spherical permanent magnet can be expressed as:

$$J_s = M\vec{z}\vec{r} = M\sin\theta'\varphi' \tag{4}$$

Based on Eq. (2), the equivalent circular current density on the surface of the spherical magnet can be calculated using the Eq. (5).

$$J_s ds = Mr'\sin^2\theta'(-r'\theta'\sin\varphi' i + r'\theta'\cos\varphi' j + k) d\varphi' d\theta' \tag{5}$$

In addition, the distance R between points A and P can be calculated by Eq. (6).

$$R = (rsin\theta\cos\varphi - r'\sin\theta'\cos\varphi')i + (rsin\theta\sin\varphi - r'\sin\theta'\sin\varphi')j$$

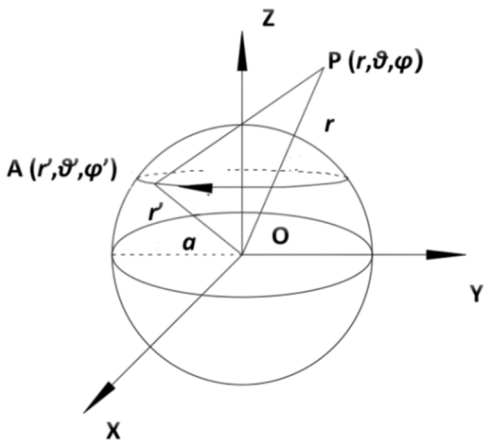

Fig. 2. Spherical magnet spatial magnetic field.

$$+ (r\cos\theta - a\cos\theta')k \tag{6}$$

Notably, the surface current density is zero at the poles and reaches its maximum along the equator, forming a ring centered on the sphere's radius. Combined Eqs. (2), (5) and (6), the magnetic flux density at Point P can be determined. To further refine the analysis, the magnetic flux density is decomposed into three directional components and integrated to obtain the values at Point P as shown in Eq. (7).

$$B_x = \frac{\mu_0 M}{4\pi} \int_0^{\pi} \times \int_0^{2\pi} \frac{r'^3 \sin^3\theta' \cos\varphi' (r\cos\theta - r'\cos\theta')}{\{r^2 + r'^2 - 2rr'[\cos\theta\cos\theta' + \sin\theta\sin\theta'\cos(\varphi - \varphi')]\}^{3/2}} d\varphi' d\theta'$$

$$B_y = \frac{\mu_0 M}{4\pi} \int_0^{\pi} \times \int_0^{2\pi} \frac{r'^3 \sin^3\theta' \cos\varphi' (r\cos\theta - r'\cos\theta')}{\{r^2 + r'^2 - 2rr'[\cos\theta\cos\theta' + \sin\theta\sin\theta'\cos(\varphi - \varphi')]\}^{3/2}} d\varphi' d\theta'$$

$$B_z = \frac{\mu_0 M}{4\pi} \int_0^{\pi} \times \int_0^{2\pi} \frac{r'^3 \sin^3\theta' [r'\sin\theta - r\cos\theta\cos(\varphi - \varphi')]}{\{r^2 + r'^2 - 2rr'[\cos\theta\cos\theta' + \sin\theta\sin\theta'\cos(\varphi - \varphi')]\}^{3/2}} d\varphi' d\theta' \tag{7}$$

For computational efficiency in magneto-fluid coupling calculations, the magnetic field intensity $\boldsymbol{H}$ is derived from the magnetic flux density using the relationship $\boldsymbol{B}=\mu_0\boldsymbol{H}$ [45].

2.3. Finite element analysis

As the magnetic field generated by the magnet significantly influences the viscosity of the polishing slurry, thereby affecting the flow field, a three-dimensional (3D) magnetic flow coupling model was developed and solved using COMSOL Multiphysics software [46].

2.3.1. Assumptions

The permanent magnet within the polishing needle was modeled as uniformly magnetized with a constant magnetization vector.
The flow of the polishing slurry was assumed to be incompressible and laminar.
The orientation and distribution of these clusters were assumed to be statistically uniform across the working gap under steady state conditions.
Since the particle dimensions were orders of magnitude smaller than the key geometric feature of the process, the polishing slurry was

approximated as a continuous and homogeneous medium for both flow and magnetic field analysis.

A one-way coupling scheme was adopted. The magnetic field dictates the fluid's rheological properties and flow, while the reverse influence of the fluid flow on the magnetic field was neglected.

2.3.2. Governing equations

Taking into account the above assumptions, the governing equations that form the basis of the simulations used in this study are detailed as follows. The magnetization form of Ampere-Maxwell Law [47] was employed to model the magnetic field distribution generated by the permanent magnets within the polishing needle. This is expressed as:

$$\nabla \bullet \boldsymbol{H} = \boldsymbol{J} + \frac{\partial \boldsymbol{D}}{\partial t} \tag{8}$$

Where $\boldsymbol{J}$ is the current density and $\boldsymbol{D}$ is the electric flux density. The flow of the polishing fluid was modeled using the Navier-Stokes equations [48], which govern the conservation of mass and momentum. These are expressed as:

$$\frac{\partial u}{\partial t} + (\boldsymbol{u} \bullet \nabla)\boldsymbol{u} = \frac{1}{\rho}(-\nabla p + \nabla \cdot (\eta \nabla \boldsymbol{u}) + (\boldsymbol{J} \times \boldsymbol{B})$$

$$\nabla \bullet \boldsymbol{u} = 0 \tag{9}$$

Where $\boldsymbol{u}$ and p are the non-dimensional velocity vector and kinetic pressure, respectively. ρ is the density of the fluid.

2.3.3. Simulation model

As illustrated in Fig. 3(a), the model geometry comprises a 304 stainless steel workpiece, which is a tube with a 4 mm inner diameter and 32 mm length, filled with polishing slurry. This assembly is surrounded by a central magnet array and a spherical air domain of 30 mm radius that defines the computational boundary. The magnets were specified as N35 grade NdFeB with a residual magnetic flux density of 1.2 T. For the numerical simulation, a free tetrahedral mesh was adopted to discretize the computational domain. To accurately resolve the high-gradient flow regions adjacent to solid surfaces, a refined boundary-layer mesh was implemented near all fluid–solid interfaces. Regarding the boundary conditions, the outer boundary of the surrounding air domain was set as magnetically insulated for the magnetic field analysis. In the fluid dynamics simulation, the inner surface of the tube was modeled as a stationary no-slip wall, while the surface of the polishing needle was specified as a rotating wall. This study systematically analyzed the effects of two magnetization methods and five magnet shapes, shown in Fig. 3(b-c), on the system's performance. The distributions of magnetic flux density, linear velocity, and magnetization pressure on the inner surface were evaluated. Additional simulation parameters are summarized in Table 1 and magnet dimensions are provided in Table 2.

Table 1
FE Simulation conditions.

Parameters (unit)	Magnet	Workpiece	Polishing slurry
Relative permeability	1	1	1.05
Density (kg/m^3)		8940	3030
Parameters (unit)	**Value**		
Polishing gap H (mm)	1		
Rotation speed V (rpm)	500–1600		

2.4. Experimental setup and characterization

The experimental setup for inner surface polishing of slender tubes is illustrated in Fig. 4. As shown in Fig. 4(a), the workpiece was securely held in place on a stage using a fixture. The stage is capable of precise movement along both the x and y axes, facilitated by a motor and linear guides. Positioned above the workpiece, a spindle is connected to the polishing needle, allowing for controlled rotation during the polishing process. The polishing gap between the polishing needle and inner surface of the workpiece is adjusted by controlling the x and y axes.

Before polishing, polishing slurry was first introduced into the tube, followed by the insertion of the polishing needle, as shown in Fig. 4(b). For these experiments, a 304 stainless steel tube with a length-to-diameter ratio of 25:1 and a total length of 100 mm was selected as the workpiece. The initial surface roughness (Ra) of inner surface was around 1.29 μm. The polishing slurry consisted primarily of CIP with an average particle size of 5 μm, and alumina (Al_2O_3) abrasives averaging 3 μm, suspended in deionized water. To ensure effective polishing, the polishing slurry was changed every 15 min. The gaps between the outer surface of the polishing needle and the inner wall of the tube were set at approximately at 0.75 and 1.0 mm. The spindle was operated at a constant rotation speed of 900 rpm. The 115 mm flexible polishing needle, shown in Fig. 4(c), was constructed from multiple neodymium iron boron (NdFeB, N35) magnets. The shape and dimensions of the magnets used in the polishing needle matched those specified in the simulation model described above. Meanwhile, the magnet arrangement and rotational speed used in the experiments were selected based on the

Table 2
Dimensions of different shape magnets.

Item	c (mm)	a (mm)	b (mm)
Shape-1	2	1	2
Shape-2	2	1	1
Shape-3	2	2	1
Shape-4	2	2	3
Sphere	2	2	2

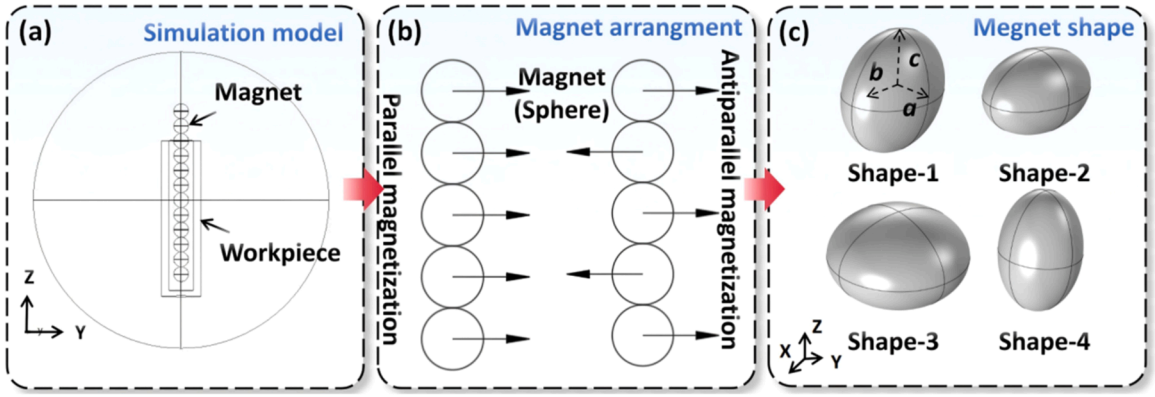

Fig. 3. FE simulation. (a) Side view of FE simulation model. (b) Magnetization method. (c) Magnet shapes.

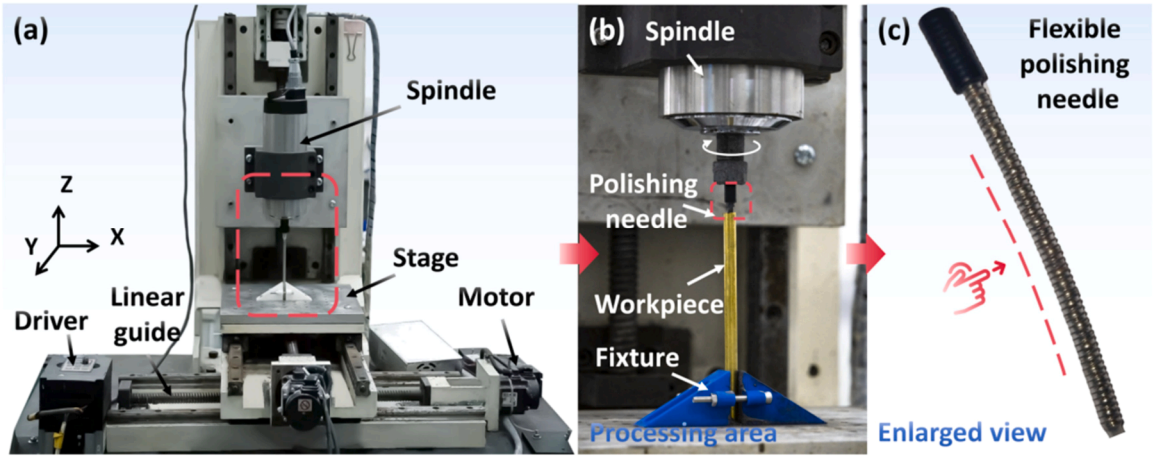

Fig. 4. Experimental setup for polishing slender tube. (a) Photograph of experimental platform. (b) Enlarged view of processing area. (c) Photograph of flexible polishing needle.

optimal conditions predicted by the simulations. The detailed experimental conditions are provided in Table 3.

After polishing, the workpiece was cleaned using absolute ethanol as the cleaning medium in an ultrasonic cleaner for 5 min. The surface topography before and after polishing was observed with a metallurgical microscope (AOSVI M230). Surface roughness was evaluated by measuring the arithmetic average roughness (Ra) using a portable surface roughness tester (Mitutoyo SJ-210). To minimize random errors, surface roughness was measured at five different points. Error bars representing standard deviations are included in the figures to demonstrate the repeatability of the results. Additionally, the surface profile was assessed with a stylus profilometer (Form Talysurf 200).

To ensure accurate material removal analysis, a rigorous drying protocol was implemented prior to weight measurement. Following cleaning, the workpiece was immediately placed into an electric-heated thermostatic drying oven. It underwent continuous drying at 70°C for one hour to actively remove moisture. Subsequently, the workpiece remained undisturbed inside the switched-off oven for at least one additional hour. This step allowed for the complete evaporation of any residual moisture and ensured the sample reached thermal equilibrium with the ambient environment, thereby eliminating potential measurement errors. The material removal rate (MRR) was determined by calculating the difference in the workpiece's weight before and after polishing, which calculated by Eq. (10). Weight measurements were performed with an electronic balance with a resolution of 0.1 mg.

$$MRR = \frac{w_b - w_a}{w_b} \tag{10}$$

Where, w_b and w_a are the workpiece's weight before and after polishing, respectively.

Table 3
Detailed experimental conditions.

Parameter (unit)	Value
Polishing time T (min)	0–90
Polishing gap H (mm)	0.75 and 1
Polishing slurry composition	**Weight percentage**
CIP	52%
Al_2O_3 particles	14%
Deionized water	30%
Anionic dispersant	3%
α-cellulose	1%

3. Results and discussion

3.1. Simulation results of magnet arrangement

Fig. 5 presents the simulation results of the magnetic field and polishing fluid behavior under different magnetization conditions. Under parallel magnetization, as shown in Fig. 5(a), the magnetic flux density remains consistently high and uniform along the length of the polishing needle, ranging from 0.08 T to 0.14 T. This uniformity ensures that the CIPs form magnetic chains of similar length and thickness at all times and locations. Correspondingly, Fig. 5(b) shows that the linear velocity of the polishing fluid is evenly distributed, with peak values around 1.4×10^{-4} m/s. The linear velocity distribution reflects the flow state of the polishing slurry along the tube wall. This uniform flow supports effective and consistent material removal over the entire inner surface. The magnetization pressure, depicted in Fig. 5(c), is also distributed evenly, reaching a maximum of 369 Pa. This indicates that a uniform magnetic field generates nearly constant contact pressure, leading to an almost constant abrasive indentation depth on the workpiece surface. Consequently, the polishing fluid maintains stable behavior along the entire tube.

In contrast, the results for antiparallel magnetization, shown in Fig. 5 (d-f), reveal less uniformity. Fig. 5(d) indicates that the magnetic flux density under this condition varies more widely, from 0.02 T to 0.12 T, with a sharper decline at the tube edges. This leads to weaker magnetic confinement of the polishing fluid near the ends, potentially reducing polishing effectiveness in these regions. Fig. 5(e) demonstrates that the linear velocity of the polishing fluid is more variable, with both higher and lower velocity zones and a maximum value of about 1.2×10^{-4} m/s. This uneven flow can compromise the uniformity of material removal. Additionally, Fig. 5(f) shows that the magnetization pressure fluctuates more significantly along the tube, reaching up to 408 Pa, which may result in inconsistent polishing across the inner surface.

Building on these findings, further COMSOL analysis was conducted to assess the shear rate of the polishing slurry under different magnetization configurations and rotation speeds. As illustrated in Fig. 6(a), antiparallel magnetization produces a higher average shear rate ($0.31\ s^{-1}$) compared to the parallel arrangement ($0.11\ s^{-1}$), indicating a greater potential for material removal. However, the variation in shear rate is also much higher, making it difficult to maintain consistent surface quality. Fig. 6(b) explores the effect of rotation speed on shear rate under parallel magnetization, with peak values observed near 900 r/min. These results highlight the importance of both magnetization configuration and rotation speed in determining the shear rate of the polishing slurry, which directly impacts the overall polishing

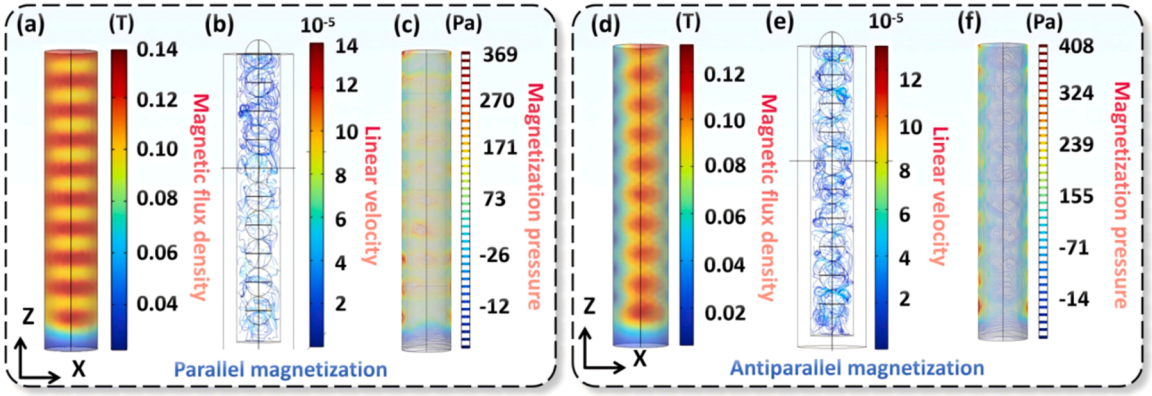

Fig. 5. Simulation results of magnet arrangement. Distribution of (a) magnetic flux density of the polishing needle, (b) Polishing fluid linear velocity and (c) magnetization pressure on inner surface of workipece under the parallel magnetization condition. Distribution of (d) magnetic field density of the polishing needle, (e) Polishing fluid linear velocity and (f) magnetization pressure on inner surface of workpiece under the antiparallel magnetization condition.

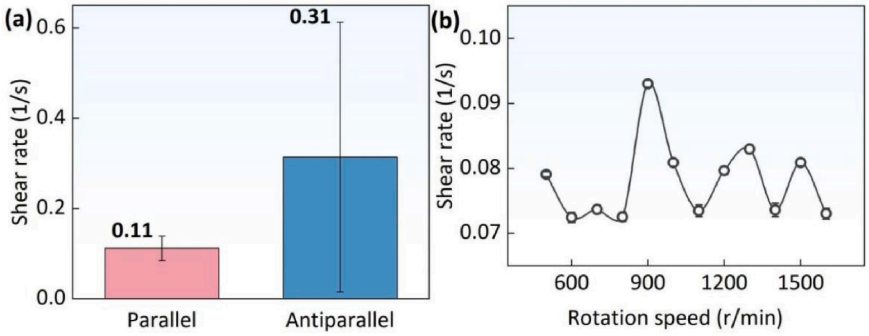

Fig. 6. Shear rate of polishing slurry on polished inner surface under different conditions. (a) Average shear rate value on polished inner surface under different magnetization conditions. (b) Variation of shear rate under different rotation speeds using parallel magnetization method.

performance for the inner surface of slender tubes.

In summary, these simulation results demonstrate that parallel magnetization provides a more uniform distribution of magnetic field, fluid velocity, and pressure along the tube. This uniformity is beneficial for achieving consistent and effective polishing of the inner surface of slender tubes. In addition, the simulations show that the shear rate reaches its maximum at 900 rpm, indicating a higher material removal capability. Therefore, the subsequent polishing experiments were conducted using the parallel magnetization configuration at a rotational speed of 900 rpm.

3.2. *Effect of polishing time and gap on polishing performance*

The influence of polishing time and the gap on the polishing performance was investigated. As shown in Fig. 7(a), the material removal increases rapidly during the initial stage of polishing for both gap sizes ($H = 0.75$ mm and $H = 1$ mm). After the first 10 min, the rate of increase slows, indicating that most material is removed early in the process. Notably, a larger gap ($H = 1$ mm) consistently results in a higher MRR compared to the smaller gap.

Fig. 7(b) illustrates how surface roughness changes with polishing time for both gap sizes. As polishing progresses, surface roughness decreases noticeably, with the greatest improvement occurring within the first 10 min. After 20 min, the surface roughness stabilizes, and the larger gap results in a slightly smoother finish. To assess the effect of longer polishing duration, Fig. 7(c) shows the surface roughness over an extended period at a gap of 1 mm. The Ra value continues to decline, reaching its minimum after 80 min, although the rate of improvement slows with time. Fig. 7(d) provides a comparison of filtered profiles using a Gaussian filter at different polishing times. The data indicates that the surface becomes increasingly smooth as polishing time increases, with significant reductions in surface irregularities observed after 15 and 60 min.

Fig. 8 shows the surface morphology of the tube before and after polishing with a 1 mm polishing gap. As seen in Fig. 8(a), the initial surface is rough and features numerous machining marks. After 15 min of polishing, these marks become noticeably shallower, as illustrated in Fig. 8(b). With continued polishing for 60 min, most of the processing marks are effectively removed, as shown in Fig. 8(c). However, the surface does not yet exhibit a glossy finish. This suggests that while the proposed polishing needle is effective for polishing the inner tube surface, further optimization of the magnet shape and arrangement is still necessary.

Overall, a larger polishing gap improves surface finish by facilitating slurry flow, whereas extending polishing time provides rapidly diminishing improvements after an initial phase of significant roughness reduction.

3.3. *Magnet shape optimization*

To further improve polishing performance, Fig. 9 presents the simulated distributions of magnetic flux density for four different magnet shapes under both parallel and antiparallel magnetization conditions. In the case of parallel magnetization, as shown in Fig. 9(a-d), each magnet shape produces a distinct magnetic field pattern within the tube. Shape-1 and Shape-4 generate more pronounced variations in magnetic flux density along the tube length, while Shape-2 and Shape-3 result in relatively uniform field distributions. Notably, Shape-3 produces the most uniform magnetic flux density, which can be attributed to its flat geometry that allows for a greater number of magnets to be

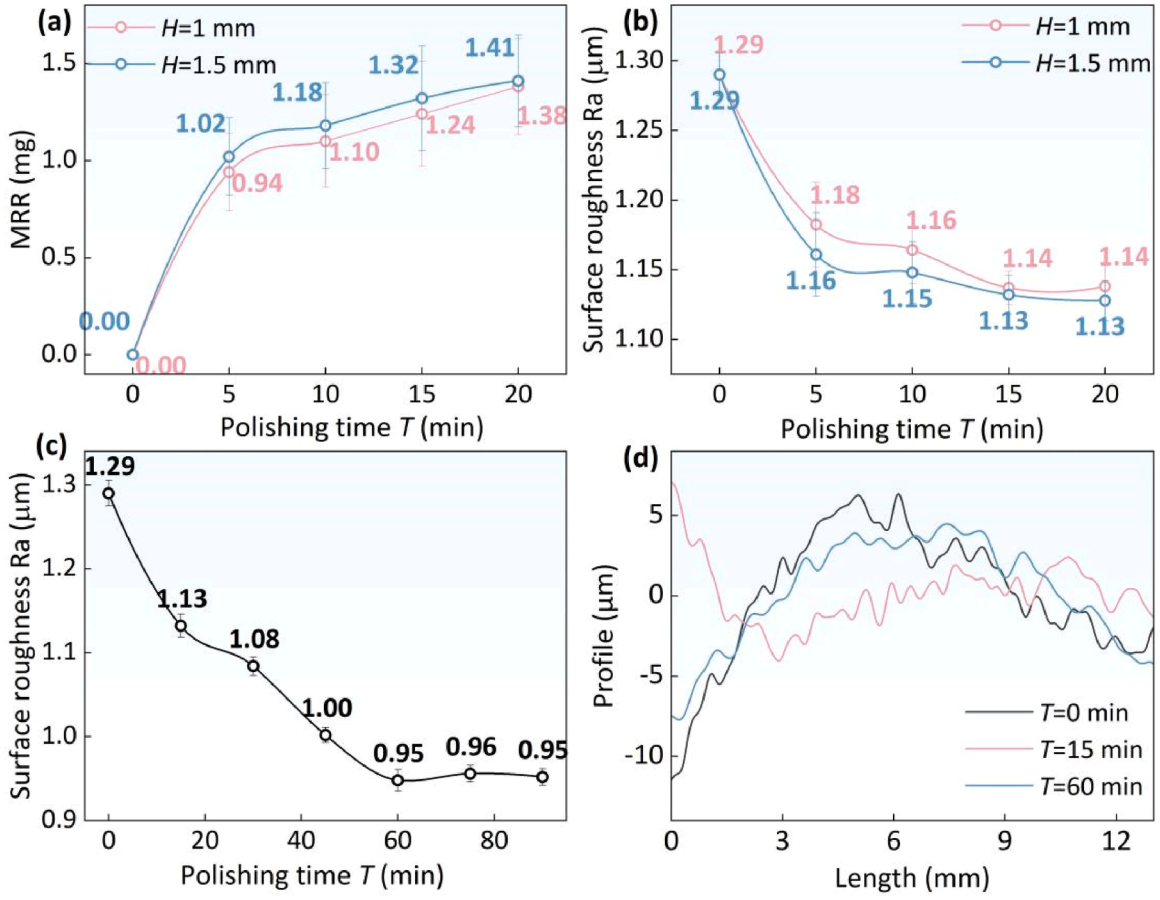

Fig. 7. Statistic analysis on polishing performance under various conditions. (a) MRR and (b) surface roughness changing with polishing time at polishing gap of 0.75 and 1 mm. (c) The surface roughness changed with polishing time at H= 1 mm. (d) Filtered profile of inner surface before and after polishing at H= 1 mm.

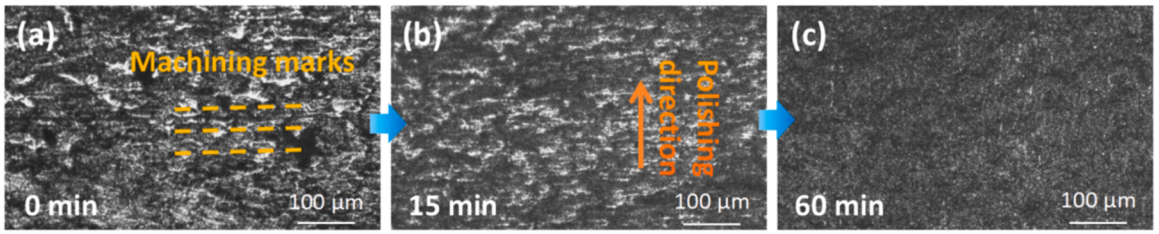

Fig. 8. Polishing performance on slender tube at H= 1 mm. Surface morphology of slender tube (a) before and after polishing (b) 15 min and (c) 60 min.

packed along the same length of the polishing needle. This design leads to a more even magnetic field, supporting stable polishing slurry behavior and consistent polishing performance. Shape-4, on the other hand, achieves the highest maximum flux density, reaching up to 0.16 T, which may enhance the magnetic control of the polishing slurry during polishing.

Under antiparallel magnetization, illustrated in Fig. 9(e-h), the magnetic field distributions become less uniform for all magnet shapes. The flux density generally decreases compared to the parallel arrangement, with more significant fluctuations observed along the tube. Shape-4 continues to provide the highest peak flux density, while the other shapes exhibit lower and more variable field strengths.

Table 4 summarizes the effects of magnet shape and arrangement on average shear rate. All four new magnet shapes produced higher average shear rates than the original spherical magnets, indicating improved potential for material removal. However, Shape-1 and Shape-2, despite their high average shear rates, also showed large standard deviations, making it difficult to achieve uniform polishing. Shape-3 stood out by combining an increased average shear rate with a much lower standard deviation, suggesting it is more effective for both efficient and uniform polishing.

Further experimental analysis of MRR and surface roughness for each magnet shape is presented in Fig. 10. All shapes reached their highest MRR within the first 15 min, with Shape-2 and Shape-3 achieving the greatest peak values. Over time, MRR decreased for all shapes. In terms of surface roughness, Shape-3 demonstrated the most significant improvement, achieving the lowest surface roughness value of 0.45 μm after 30 min, outperforming both the other shapes and the original spherical magnets.

Finally, Shape-3 magnets were used to polish the inner surface of the tube, and the results are shown in Fig. 11. As polishing time increases, the machining marks on the inner wall are progressively removed. After 30 min, the surface appears significantly smoother, with most of the initial machining marks eliminated as shown in Fig. 11(c-d). Compared to the results achieved with spherical magnets, the polishing effect using Shape-3 is markedly improved, demonstrating enhanced surface quality

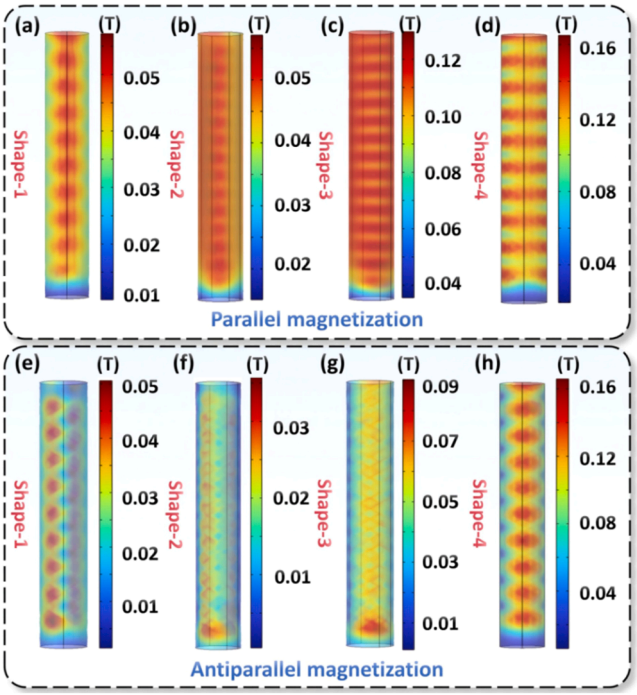

Fig. 9. Distribution of magnetic flux density using various magnet shapes and arrangements. (a) Shape-1, (b) Shape-2, (c) Shape-3 and (d) Shape-4 under the parallel magnetization condition. (e) Shape-1, (f) Shape-2, (g) Shape-3 and (h) Shape-4 under the antiparallel magnetization condition.

Table 4
Effect of various magnet shape and arrangement on average shear rate.

Item	Magnetization method	Average shear rate (1/s)	Standard deviation
Shape-1	Parallel	0.43	0.21
	Antiparallel	0.73	0.38
Shape-2	Parallel	0.36	0.17
	Antiparallel	0.83	0.31
Shape-3	Parallel	0.20	0.04
	Antiparallel	0.34	0.04
Shape-4	Parallel	0.15	0.08
	Antiparallel	0.12	0.01
Sphere	Parallel	0.11	0.03
	Antiparallel	0.31	0.29

and more effective removal of imperfections.

4. Verification on slender bend tubes

Building on previous experimental findings and the optimized magnet configuration, validation tests were performed using the proposed polishing needle on 304 stainless steel tubes with six different bend angles (15°, 30°, 45°, 60°, 75°, and 90°), as shown in Fig. 12(a). The evaluation focused on both the straight and bend sections of each tube, examining surface morphology, roughness, and flow characteristics. The experimental setup for polishing these slender bent tubes is shown in Fig. 12(b). To ensure a uniform finish across the interior circumference, a synchronized counter-rotation strategy was employed. The tube is mounted on a rotary stage that rotates slowly in one direction along its axis, while the polishing needle rotates at high speed in the opposite direction. This dual-rotation system is designed to minimize deviations in tool alignment over time, thereby improving the consistency of material removal and surface quality around the entire inner circumference. As depicted in Fig. 12(c), flow rate tests were conducted using a solution of α-cellulose and water with a viscosity of 4 cps. The experimental setup utilized 3D-printed fixtures to ensure consistent tube

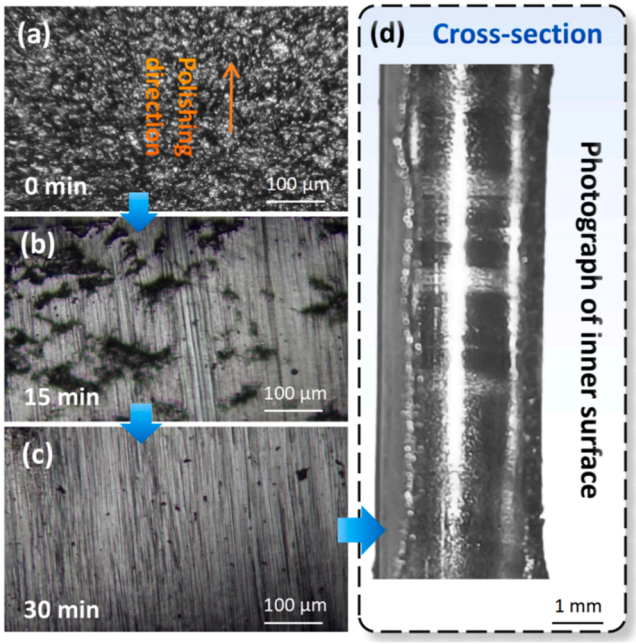

Fig. 11. Surface morphology of inner surface before and after polishing by using shape-3 magnet. (a) $T = 0$ min. (b) $T = 15$ min. (c) $T = 30$ min. (d) Photograph of the inner surface after polishing 30 min.

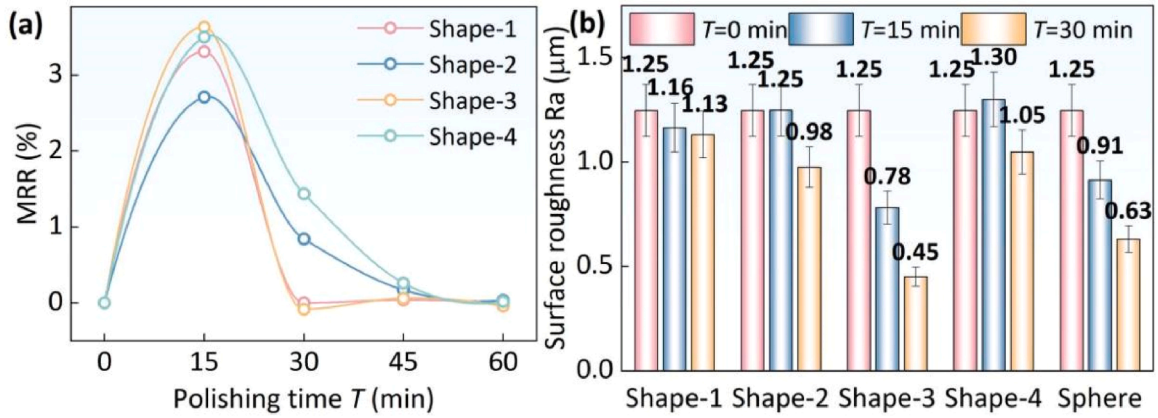

Fig. 10. Effect of magnet shape on polishing performance. (a) MRR changing with polishing time. (b) Summary of surface roughness using different magnet shapes.

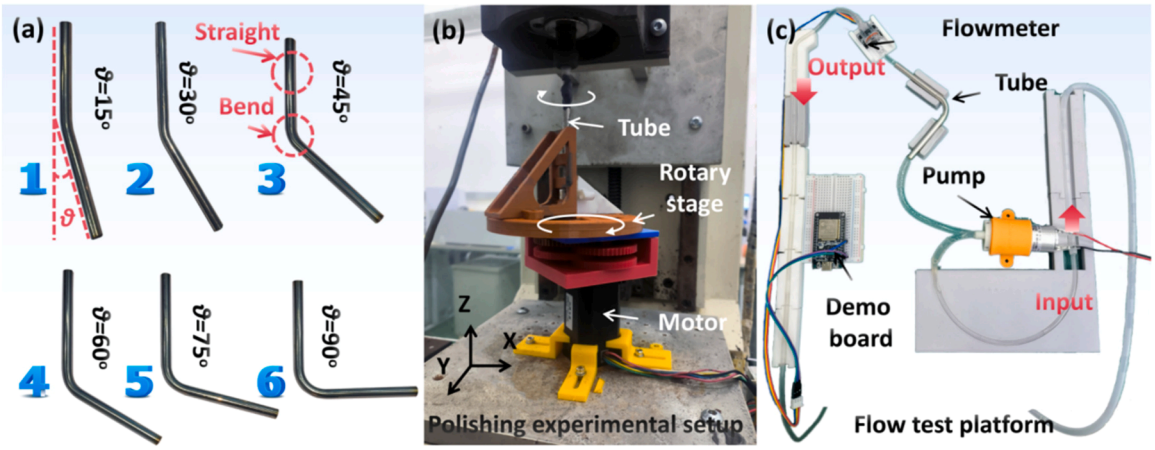

Fig. 12. Verification experiments on various types of slender bend tube. (a) Photograph of slender bend tube. (b) Polishing experimental setup. (c) Flow test platform.

positioning and length. Flow rates were measured by recording the time required for the solution volume to decrease from 1000 mL to 600 mL, both before and after polishing.

Fig. 13(a-f) present the surface morphology of tubes with varying bend angles following a 30 min polishing process at straight sections. For tubes with smaller bend angles, the inner surfaces exhibit a significantly smoother finish, as shown in Fig. 13(a-c). As the bend angle increases, the polished surfaces show more residual scratches and a corresponding decline in finish quality, visible in Fig. 13(d-f). This trend is quantitatively supported by surface roughness measurements taken before and after polishing. Prior to polishing, the initial value of the straight sections ranged from 1.24 to 1.32 μm, while the bend sections were rougher, measuring between 1.93 and 2.28 μm. After the 30 min polishing, the surface roughness of the straight sections was reduced to 0.40–0.62 μm. Similarly, the bend sections showed significant improvement, with values decreasing to 0.54–0.62 μm. These results confirm a substantial enhancement in inner surface quality for all tube types, while also indicating that achieving a uniform finish becomes more challenging as the tube geometry becomes more complex.

Beyond surface measurements, the functional benefit of this roughness improvement was evaluated through flow rate testing. Fig. 14(a-f) present the flow rate results for tubes with varying bend angles. In all cases, polished tubes demonstrated higher flow rates compared to unpolished tubes, with the maximum increase approaching 20%. These

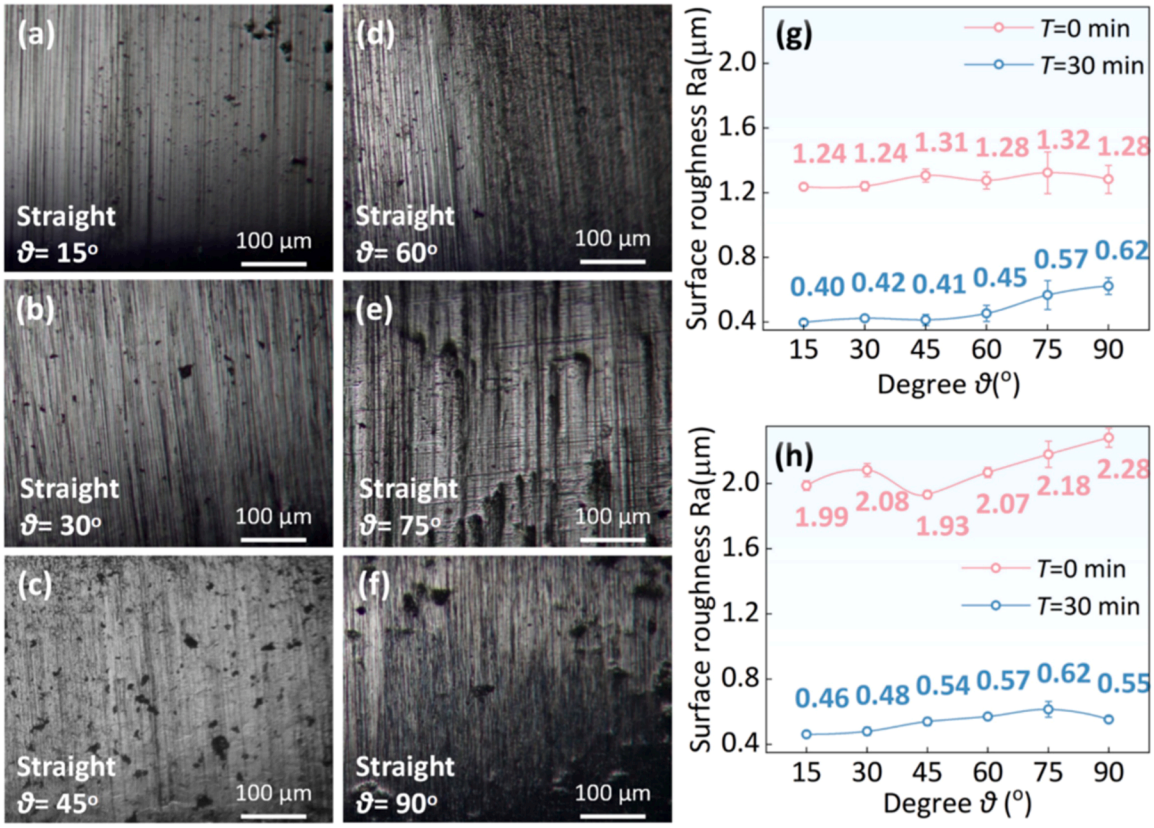

Fig. 13. Polishing performance on on various types of slender bend tube. Surface morphology of (a) 15°, (b) 30°, (c) 45°, (d) 60°, (e) 75° and (f) 90° slender bend tube at straight section after 30 min polishing. Surface roughness of (g) straight and (h) bend sections before and after polishing.

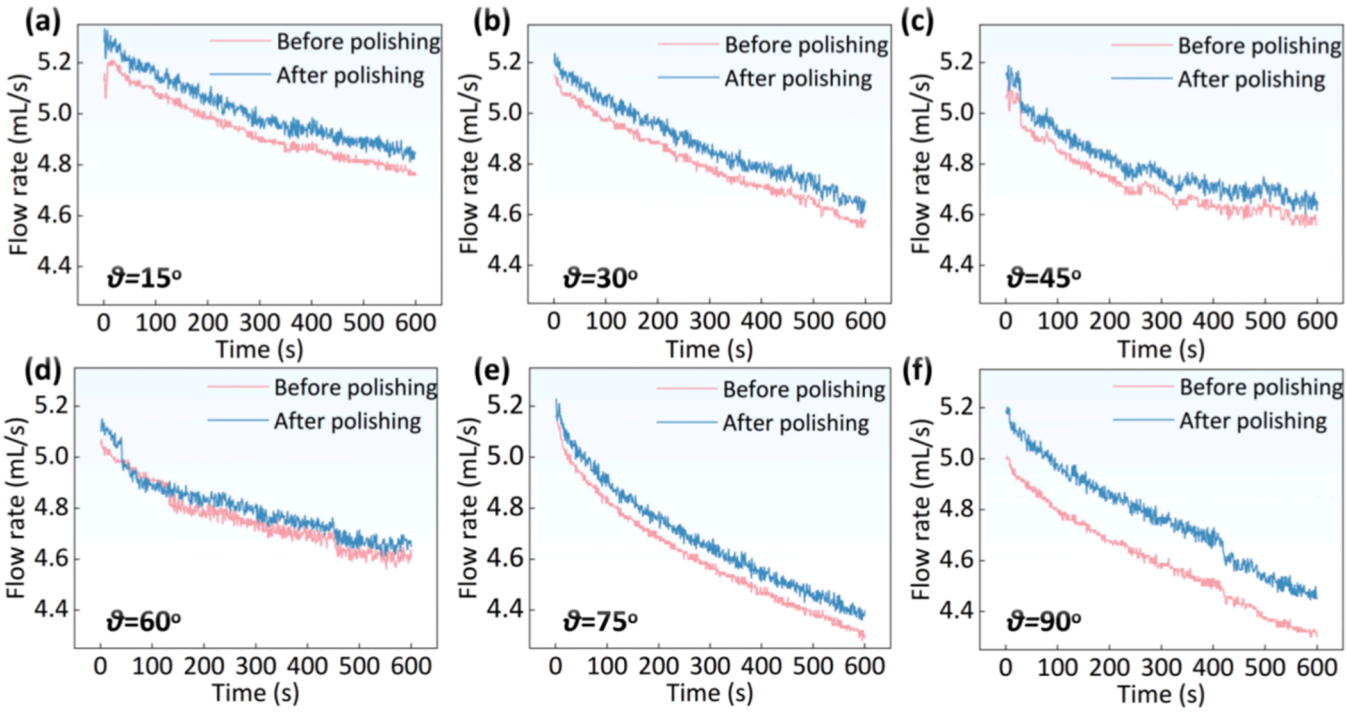

Fig. 14. Flow rate of bend tube before and after polishing. Flow rate of (a) 15°, (b) 30°, (c) 45°, (d) 60°, (e) 75° and (f) 90° slender bend tube before and after polishing.

findings indicate that improved inner surface quality effectively reduces fluid retention and enhances flow efficiency.

It is noteworthy that the polishing performance in the bend sections of the tubes is inferior to that in the straight sections. As shown in Fig.s 15(a-b), a significant number of machining marks remain on the inner surfaces of tubes with 75° and 90° bends, even after 30 min of polishing. This observation is further supported by the surface roughness measurements presented in Fig. 13(a-b), which indicate higher roughness values in the bend regions. One contributing factor to this reduced polishing effectiveness is the decrease in shear rate within the polishing

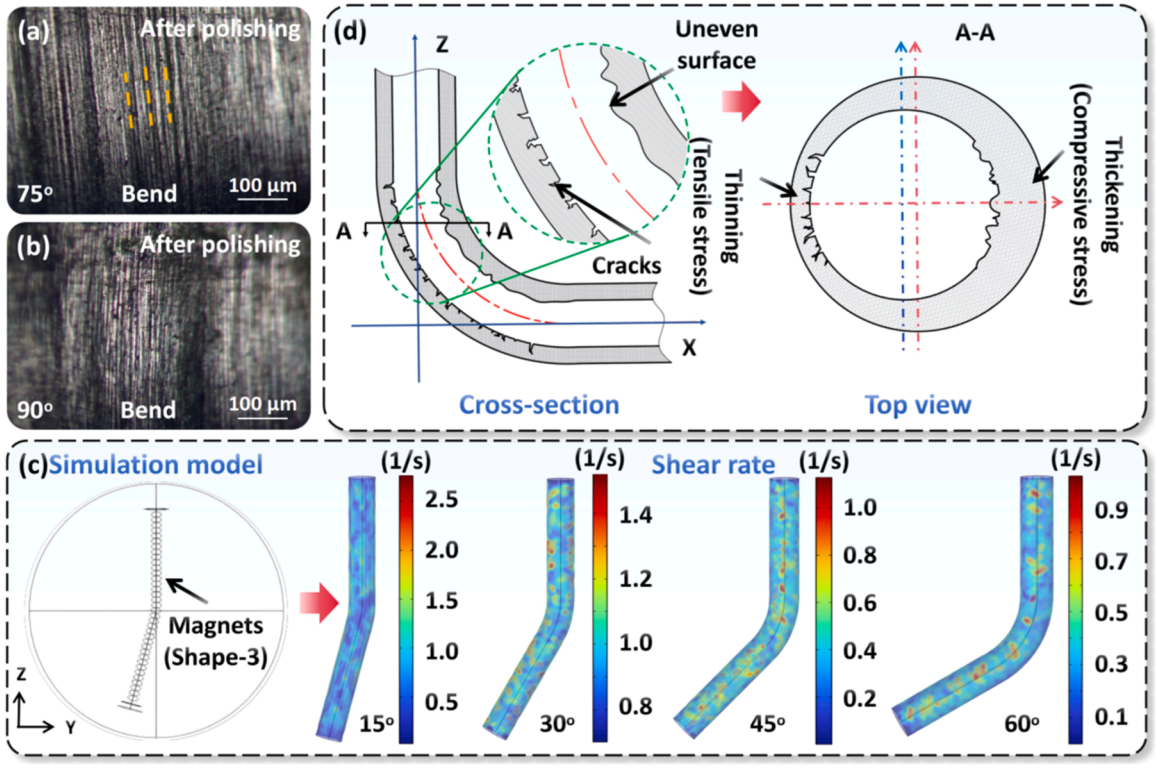

Fig. 15. Polishing performance at the bend section. Surface morphology of tubes with (a) 75° and (b) 90° bend angles after 30 min of polishing. (c) Simulation results showing the shear rate in tubes with different bend angles. (d) Schematic illustration of the bend section.

slurry as the bend angle increases. FE simulations, illustrated in Fig. 15 (c), demonstrate that both the magnitude and uniformity of the shear rate decline with larger bend angles. This reduction is primarily due to the complex geometry of the bend, which impedes the rotational motion and flow of the polishing slurry inside the tube, thereby diminishing the overall polishing action.

Additionally, the mechanical deformation that occurs during tube bending further complicates the polishing process. As depicted in Fig. 15 (d), the outer wall of the bend experiences tensile stress, leading to wall thinning and the formation of cracks, while the inner wall is subjected to compressive stress, resulting in wall thickening and an uneven surface. These structural changes increase the initial surface roughness in the bend sections compared to the straight sections, as also evidenced in Fig. 13(b). Furthermore, inherent flexibility of the polishing needle, combined with dynamic fluid forces, can still generate a degree of eccentricity during operation, which impacts the ideal uniform gap.

Future research should focus on further optimizing both the design of the polishing needle and the formulation of the polishing fluid to address the challenges identified in the bend sections. For instance, tailoring the flexibility and geometry of the polishing needle may enhance its adaptability to complex tube shapes, thereby improving contact and polishing efficiency in bend regions. Additionally, adjusting the composition and rheological properties of the polishing slurry could help maintain a higher and more uniform shear rate, even in areas with severe bends. These improvements have the potential to significantly enhance the overall surface quality of slender bent tubes. Importantly, the findings from this study also provide reference for polishing inner surface of slender bend tubes.

5. Conclusions

This study addresses the challenge of precision polishing for the inner surfaces of slender tubes by developing a novel flexible polishing needle that utilizes magnets constrained by a coil spring. The key findings of this research are summarized as follows:

(1) A novel polishing needle, composed of magnets constrained by a coil spring, was designed to effectively adapt to complex tube geometries and enable efficient inner surface polishing.
(2) The shape and arrangement of the magnets were systematically optimized through finite element (FE) simulations and experimental validation. Simulation results demonstrated that parallel magnetization yields a more uniform magnetic flux density and fluid velocity distribution, thereby supporting consistent material removal and enhanced polishing performance.
(3) The proposed method was successfully applied to tubes with various bend angles. The average surface roughness of the inner tube surfaces was reduced from initial values of 1.24–2.28 μm to as low as 0.40–0.62 μm after 30 min polishing, in both straight and curved sections.
(4) The polishing needle exhibited excellent performance in tubes with bend angles ranging from 15° to 90°, consistently achieving significant improvements in surface quality and flow efficiency.

In summary, the proposed polishing method significantly enhances both the surface finish and fluid transport performance of slender bent tubes, underscoring its potential for practical applications in advanced manufacturing.

CRediT authorship contribution statement

Dawei Gao: Writing – review & editing, Project administration, Methodology, Investigation. **Yifan Xu:** Writing – original draft, Investigation. **Chen Jiang:** Writing – review & editing, Project administration, Methodology, Funding acquisition. **Rui Gao:** Writing – review & editing, Investigation.

Declaration of Competing Interest

The authors declare that they have no known competing financial interests or personal relationships that could have appeared to influence the work reported in this paper.

Acknowledgements

This work was supported by the National Natural Science Foundation of China (Project codes: 52175239, 51475310) and State Key Laboratory of Mechanical System and Vibration (Project code: MSV202315).

Data availability

Data will be made available on request.

References

[1] J. Guo, Q.K. Li, Z. Tong, W.S. Zhao, L. Li, A new internal surface polishing method for sub-millimeter slender tube with varying diameters, CIRP Ann. Manuf. Techn. 73 (2024) 265–268, https://doi.org/10.1016/j.cirp.2024.04.031.
[2] J.Y. Li, Z.H. Fan, Z.H. Yang, Y.B. Tian, J. Gao, Simulation and modeling of magnetorheological shear thickening polishing processes for slender tube, J. Mater. Res Technol. 25 (2023) 480–496, https://doi.org/10.1016/j.jmrt.2023.05.226.
[3] Z.Y. Luo, C.Y. Wu, Z.Y. Jin, B. Guo, S.D. Gao, K.L. Luo, H.Y. Liu, M.J. Chen, Research on rotary magnetorheological finishing of the inner surface of stainless steel slender tubes, Micromachines 16 (2025) 763, https://doi.org/10.3390/mi16070763.
[4] X.Q. Liu, J. Zheng, J.J. Fu, J.Q. Ji, G.M. Chen, Multi-level optimization of maintenance plan for natural gas pipeline systems subject to external corrosion, J. Nat. Gas. Sci. Eng. 50 (2018) 64–73, https://doi.org/10.1016/j.jngse.2017.11.021.
[5] F. Wu, K. Zhao, X.L. Wu, H.J. Peng, L.L. Zhao, W.X. Zhong, A time-averaged method to analyze slender rods moving in tubes, Int J. Mech. Sci. 279 (2024) 109510, https://doi.org/10.1016/j.ijmecsci.2024.109510.
[6] X.J. Zhang, X.D. Zhao, B. Cheng, H.L. Wang, W.S. Li, C.Y. Feng, U. Seniuts, Design and processing behavior of large tubes with a rotating magnetic pole core-based magnetic abrasive finishing, Int J. Adv. Manuf. Tech. 130 (2024) 1693–1708, https://doi.org/10.1007/s00170-023-12754-7.
[7] Y.H. Dai, S.S. Li, M. Feng, B.Y. Chen, J.P. Qiao, Fundamental study of phased array ultrasonic cavitation abrasive flow polishing titanium alloy tubes, Materials 17 (2024) 5185, https://doi.org/10.3390/ma17215185.
[8] M. Kumar, A. Alok, V. Kumar, M. Das, Advanced abrasive-based nano-finishing processes: challenges, principles and recent applications, Mater. Manuf. Process 37 (2022) 372–392, https://doi.org/10.1080/10426914.2021.2001509.
[9] N.L. Ravikumar, K.K. Kar, D. Sathiyamoorthy, A. Kumar, R. Devi, Surface finishing of carbon-carbon composites using abrasive flow machining, Full. Nanotub Car N. 20 (2012) 170–182, https://doi.org/10.1080/1536383X.2010.533595.
[10] A.A. Gomez-Gallegos, F. Mill, A.R. Mount, Surface finish control by electrochemical polishing in stainless steel 316 pipes, J. Manuf. Process 23 (2016) 83–89, https://doi.org/10.1016/j.jmapro.2016.05.010.
[11] W.Z. Wu, J.Q. Wang, Q.P. Liu, H.C. Xiao, X.C. Li, Y.M. Zhou, H.M. Wang, A. D. Zheng, J. Zhao, L.Q. Ren, G.W. Li, Electrochemical polishing assisted selective laser melting of biomimetic superhydrophobic metallic parts, Appl. Surf. Sci. 596 (2022) 153601, https://doi.org/10.1016/j.apsusc.2022.153601.
[12] J.H. Liu, X.H. Niu, Y.Q. Jia, N. Zhan, Y.D. Zou, Y.H. Shi, J.W. Zhou, Chemical mechanical polishing for copper films in integrated circuit wiring layers using an advanced slurry, Tribol. Int. 198 (2024) 109832, https://doi.org/10.1016/j.triboint.2024.109832.
[13] C.F. Cheung, C.J. Wang, Z.C. Cao, L.T. Ho, M.Y. Liu, Development of a multi jet polishing process for inner surface finishing, Precis Eng. 52 (2018) 112–121, https://doi.org/10.1016/j.precisioneng.2017.11.018.
[14] J.D. Kim, Y.H. Kang, Y.H. Bae, S.W. Lee, Development of a magnetic abrasive jet machining system for precision internal polishing of circular tubes, J. Mater. Process Tech. 71 (1997) 384–393, https://doi.org/10.1016/S0924-0136(97)00103-9.
[15] J. Guo, K.H. Au, C.N. Sun, M.H. Goh, C.W. Kum, K. Liu, J. Wei, H. Suzuki, R. K. Kang, Novel rotating-vibrating magnetic abrasive polishing method for double layered internal surface finishing, J. Mater. Process Tech. 264 (2019) 422–437, https://doi.org/10.1016/j.jmatprotec.2018.09.024.
[16] J.Y. Li, L.F. Yang, W.N. Liu, X.C. Zhang, F.Y. Sun, Experimental research into technology of abrasive flow machining nonlinear tube runner, Adv. Mech. Eng. (2014) 752353, https://doi.org/10.1155/2014/752353.
[17] S. Wan, Y.J. Ang, T. Sato, G.C. Lim, Process modeling and CFD simulation of two-way abrasive flow machining, Int J. Adv. Manuf. Tech. 71 (2014) 1077–1086, https://doi.org/10.1007/s00170-013-5550-4.
[18] G.S. Liu, X.M. Zhang, X. Zang, J.Y. Li, N.N. Su, Study on whole factorial experiment of polishing the micro-hole in non-linear tubes by abrasive flow, Adv. Mech. Eng. 10 (2018), https://doi.org/10.1177/1687814018794590.
[19] M.S. Duval-Chaneac, S. Han, C. Claudin, F. Salvatore, J. Bajolet, J. Rech, Experimental study on finishing of internal laser melting (SLM) surface with

abrasive flow machining (AFM), Precis Eng. 54 (2018) 1–6, https://doi.org/10.1016/j.precisioneng.2018.03.006.
[20] C. Peng, Q.H. Xu, L. Ding, T.Y. Zhou, H. Gao, X.P. Wang, Novel insights into abrasive flow machining uniformity for SLM channels, Int J. Mech. Sci. 262 (2024) 108726, https://doi.org/10.1016/j.ijmecsci.2023.108726.
[21] B.C. Zhang, L. Xiaohua, J.M. Bai, J.F. Guo, P. Wang, C.N. Sun, M.L. Nai, G.J. Qi, J. Wei, Study of selective laser melting (SLM) Inconel 718 part surface improvement by electrochemical polishing, Mater. Des. 116 (2017) 531–537, https://doi.org/10.1016/j.matdes.2016.11.103.
[22] W.Z. Wu, J.Q. Wang, Q.P. Liu, X.C. Li, Y.M. Zhou, A.D. Zheng, L.Q. Ren, G.W. Li, Surface finish analysis of gradient voltage electrochemical polishing of 316L stainless steel parts forming by laser powder bed fusion, 3, D. Print. Addit. Manuf. 11 (2024) e801–e811, https://doi.org/10.1089/3dp.2022.0275.
[23] M. Barletta, S. Guarino, G. Rubino, V. Tagliaferri, Progress in fluidized bed assisted abrasive jet machining (FB-AJM): Internal polishing of aluminium tubes, Int J. Mach. Tool. Man. 47 (2007) 483–495, https://doi.org/10.1016/j.ijmachtools.2006.06.005.
[24] J. Zhao, Y.C. Xiang, C. Fan, A new method for polishing the inner wall of a circular tube with a soft abrasive rotating jet, Powder Technol. 398 (2022) 117068, https://doi.org/10.1016/j.powtec.2021.117068.
[25] J. Zhao, F.Q. Song, C. Fan, Multi-objective prediction and optimization for soft abrasive rotary jet polishing inner surface, Int J. Adv. Manuf. Tech. 134 (2024) 5355–5374, https://doi.org/10.1007/s00170-024-14420-y.
[26] R. Gao, Y.M. Loh, K.S. Li, R. Chen, C. Jiang, C.F. Cheung, C.J. Wang, Study on the material removal mechanism of cemented carbide magnetic materials in magnetic field-assisted mass polishing, Tribol. Int. 208 (2025) 110647, https://doi.org/10.1016/j.triboint.2025.110647.
[27] Y.H. Zou, H.J. Xie, C.W. Dong, J.Z. Wu, Study on complex micro surface finishing of alumina ceramic by the magnetic abrasive finishing process using alternating magnetic field, Int J. Adv. Manuf. Tech. 97 (2018) 2193–2202, https://doi.org/10.1007/s00170-018-2064-0.
[28] R. Gao, C.J. Wang, Y.M. Loh, X.L. Liang, C. Jiang, C.F. Cheung, Novel batch polishing method of ceramic cutting inserts for reducing tool wear, Chin. J. Mech. Eng. En. 37 (2024) 83, https://doi.org/10.1186/s10033-024-01069-7.
[29] G.C. Verma, P. Kala, P.M. Pandey, Experimental investigations into internal magnetic abrasive finishing of pipes, Int J. Adv. Manuf. Tech. 88 (2017) 1657–1668, https://doi.org/10.1007/s00170-016-8881-0.
[30] A. Singh, P. Singh, A. Kaushik, S. Singh, L. Singh, A. Singh, B. Ram, Comparative assessment of abrasives in magnetic abrasive finishing: an experimental performance evaluation, J. Magn. Magn. Mater. 604 (2024) 172312, https://doi.org/10.1016/j.jmmm.2024.172312.
[31] L. Zhang, Z. Huang, H.P. Shao, Y. Li, H. Zheng, Effects of γ-Fe_2O_3 on γ-Fe_2O_3/Fe_3O_4 composite magnetic fluid by low-temperature low-vacuum oxidation method, Mater. Des. 105 (2016) 234–239, https://doi.org/10.1016/j.matdes.2016.05.077.
[32] C. Jiang, J.L. Huang, Z.Y. Jiang, D.B. Qian, X.L. Hong, Estimation of energy savings when adopting ultrasonic vibration-assisted magnetic compound fluid polishing, Int J. Pr. Eng. ManGt 8 (2021) 1–11, https://doi.org/10.1007/s40684-019-00167-5.
[33] W.L. Song, Z. Peng, P.F. Li, P. Shi, S.B. Choi, Annular surface micromachining of titanium tubes using a magnetorheological polishing technique, Micro Basel 11 (2020) 314, https://doi.org/10.3390/mi11030314.
[34] H.R. Guo, Y.B. Wu, D. Lu, M. Fujimoto, M. Nomura, Effects of pressure and shear stress on material removal rate in ultra-fine polishing of optical glass with magnetic compound fluid slurry, J. Mater. Process Tech. 214 (2014) 2759–2769, https://doi.org/10.1016/j.jmatprotec.2014.06.014.
[35] X.L. Hong, C. Jiang, H. Ye, Z.Y. Jiang, J.H. Liu, L.X. Sun, Effects of magnetic compound fluid polishing on surface morphology and laser damage resistance of multilayer dielectric pulse compression gratings, Opt. Laser Technol. 192 (2025) 113543, https://doi.org/10.1016/j.optlastec.2025.113543.
[36] H. Nishida, K. Shimada, M. Goto, Polishing inner capillary walls by a magnetic compound fluid, Int J. Appl. Electro 25 (2007) 25–29, https://doi.org/10.3233/JAE-2007-850.
[37] H. Nishida, K. Shimada, Y. Ido, Investigation of polishing for inner capillary walls by MCF flow method, Int J. Appl. Electro 33 (2010) 1685–1690, https://doi.org/10.3233/JAE-2010-1301.
[38] H. Nishida, K. Shimada, Y. Ido, Effectiveness of using a magnetic compound fluid with a pulsed magnetic field for flat surface polishing, Int J. Appl. Electro 39 (2012) 623–628, https://doi.org/10.3233/JAE-2012-1520.
[39] Y.F. Xue, W.T. Zhang, Y.L. Wang, M. Feng, Y.K. Zheng, H.Q. Wu, Y.B. Wu, Inner-surface polishing of capillary tube with magnetic compound fluid slurry, Int J. Mech. Sci. 287 (2025) 109923, https://doi.org/10.1016/j.ijmecsci.2025.109923.
[40] Y.F. Xue, W.T. Zhang, H.Q. Wu, Y.K. Zheng, G.Z. Li, Y.B. Wu, Mechanistic investigation of chemically assisted magnetic compound fluid polishing of titanium capillary tube inner surfaces, Precis Eng. 97 (2026) 179–194, https://doi.org/10.1016/j.precisioneng.2025.09.012.
[41] M. Nomura, K. Ozasa, T. Fujii, T. Suzuki, Y.B. Wu, Development of ultrasonic vibration-assisted magnetic compound fluid (MCF) polishing technology, Int J. Auto. Tech. Jpn 16 (2022) 71–77, https://doi.org/10.20965/ijat.2022.p0071.
[42] D.D. Zhou, X.M. Huang, Y. Ming, X.Y. Li, H.Y. Li, W. Li, Material removal characteristics of magnetic-field enhanced shear thickening polishing technology, J. Mater. Res. Technol. 15 (2021) 2697–2710, https://doi.org/10.1016/j.jmrt.2021.09.092.
[43] S.J. Han, X.T. Han, W. Sun, The analysis of magnetic flux density inside rogowski coil based on full current theory, Ieee Sens. Lett. 4 (2020) 1–4, https://doi.org/10.1109/LSENS.2020.2987707.
[44] H.S. Lopez, F. Liu, M. Poole, S. Crozier, Equivalent magnetization current method applied to the design of gradient coils for magnetic resonance imaging, Ieee T Magn. 45 (2009) 767–775, https://doi.org/10.1109/TMAG.2008.2010053.
[45] R. Gao, D.W. Luo, Y.M. Loh, C.F. Cheung, C. Jiang, C.J. Wang, Enhancing surface integrity of medical Ti-6Al-4V alloy via magnetic field-assisted mass polishing, J. Mater. Res Technol. 34 (2025) 1068–1079, https://doi.org/10.1016/j.jmrt.2024.12.081.
[46] C.J. Wang, C.F. Cheung, L.T. Ho, K.L. Yung, L.B. Kong, A novel magnetic field-assisted mass polishing of freeform surfaces, J. Mater. Process Tech. 279 (2020) 116552, https://doi.org/10.1016/j.jmatprotec.2019.116552.
[47] N. Ida, Engineering Electromagnetics, fourth ed., New York, 2021.
[48] M.J. Ni, J.F. Li, A consistent and conservative scheme for incompressible MHD flows at a low magnetic Reynolds number. Part III: On a staggered mesh, J. Comput. Phys. 231 (2012) 281–298, https://doi.org/10.1016/j.jcp.2011.08.013.